


# Mechanochemistry for Thermoelectrics: Nanobulk $\text{Cu}_6\text{Fe}_2\text{SnS}_8/\text{Cu}_2\text{FeSnS}_4$ Composite Synthesized in an Industrial Mill

PETER BALÁŽ,<sup>1</sup> MICHAL HEGEDÜS ,<sup>2,6</sup> MIKE REECE,<sup>3</sup>  
RUI-ZHI ZHANG,<sup>3</sup> TAICHAO SU,<sup>3</sup> IVAN ŠKORVÁNEK,<sup>4</sup>  
JAROSLAV BRIANČIN,<sup>1</sup> MATEJ BALÁŽ,<sup>1</sup> MATÚŠ MIHÁLIK,<sup>4</sup>  
MATEJ TEŠÍNSKY,<sup>1</sup> and MARCELA ACHIMOVIČOVÁ<sup>1,5</sup>

1.—Institute of Geotechnics, Slovak Academy of Sciences, Watsonova 45, 04001 Košice, Slovakia. 2.—Institute of Chemistry, Faculty of Science, P. J. Šafárik University in Košice, Moyzesova 11, 04001 Košice, Slovakia. 3.—School of Engineering and Material Science, Queen Mary University of London, Mile End Road, London E1 4NS, UK. 4.—Institute of Experimental Physics, Slovak Academy of Sciences, Watsonova 47, 04001 Košice, Slovakia. 5.—Institute of Mineral and Waste Processing, Waste Disposal and Geomechanics, University of Technology, Walther-Nernst-Str. 9, 38678 Clausthal-Zellerfeld, Germany. 6.—e-mail: michal.hegedus@gmail.com

We demonstrate the use of elemental precursors Cu, Fe, Sn, and S to obtain a mawsonite ( $\text{Cu}_6\text{Fe}_2\text{SnS}_8$ )/stannite ( $\text{Cu}_2\text{FeSnS}_4$ ) composite using a solid-state process at ambient temperature in an industrial eccentric vibration mill for up to 240 min in argon atmosphere. The samples were characterized using various analytical techniques such as x-ray diffractometry, scanning electron microscopy, energy-dispersive x-ray spectroscopy, and nitrogen adsorption and magnetic measurements. For thermoelectric measurements, the properties of samples densified via spark plasma sintering were measured using standard methods needed to calculate the figure of merit. The transformation of elemental precursors to a composite mixture proceeds relatively rapidly via several intermediate steps. The kinetics of this transformation is also in good agreement with the results for the unconsumed sulfur content in the reaction mixtures and can also be correlated with the magnetization results. Based on the thermoelectric measurements of the sample milled for 240 min, the calculated figure of merit reached a value of  $zT = 0.51$  at 623 K due to a very low lattice thermal conductivity of  $0.29 \text{ W/m-K}$  and moderate power factor of  $3.3 \mu\text{W/cm-K}^2$ . The thermoelectric results obtained for the material are comparable to previously published values for pure mawsonite prepared from elements by laboratory ball milling.

**Key words:** Mawsonite/stannite composite mixture, advanced material, thermoelectric material, industrial milling, mechanochemistry

## INTRODUCTION

Thermoelectric materials have become a focus of considerable interest because of their ability to convert thermal energy directly into electrical energy. Their application will contribute to solving the problem of ever-increasing global electrical

energy consumption. To date, this demand has been satisfied using several different technologies involving burning of fuels. However, depletion of fossil fuels as well as increased  $\text{CO}_2$  emissions make burning fuels unsatisfactory. To address this, researchers are investigating alternative methods for clean, safe, and sustainable electrical energy production. One such promising source is thermoelectric generation.<sup>1–3</sup>

The origin of thermoelectricity dates back to 1821 when Seebeck discovered the thermoelectric effect,

(Received July 24, 2018; accepted January 16, 2019;  
published online January 31, 2019)

i.e., that a temperature difference across a joint of two different types of wire results in a potential difference between them. Its value is directly proportional to the Seebeck coefficient  $\alpha$ , which together with the electrical conductivity  $\sigma$ , total thermal conductivity  $\kappa$ , and absolute temperature  $T$  can be used to define a dimensionless thermoelectric figure of merit  $zT$  that is used as a measure of the thermoelectric performance of a material  $zT = \alpha^2\sigma/\kappa T$ .<sup>4,5</sup> To obtain high values of  $zT$ , both the Seebeck coefficient and electrical conductivity must be large, while the thermal conductivity (including carrier and lattice contributions) must be minimized. This is why materials with low  $\kappa$  are especially interesting as potential candidate thermoelectrics.

Among low- $\kappa$  materials, the ternary sulfide tetrahedrite  $\text{Cu}_{12}\text{Sb}_4\text{S}_{13}$  represents an extraordinary thermoelectric material that has been studied recently in great detail.<sup>6–12</sup> Tetrahedrite is a natural mineral which has been treated in metallurgy as a potential source of copper.<sup>13,14</sup> The application of tetrahedrite as a suitable thermoelectric material is based on its Earth-abundant composition, predisposition to incorporate other metals into its crystal structure as dopants, and in particular its low thermal conductivity. Other Cu-based compounds have also been frequently reported as good thermoelectric materials for use in the intermediate temperature range (300°C to 600°C).<sup>11,15–22</sup> Cu-based compounds show high thermoelectric performance, as well as offering many other advantages such as Earth abundance, environmental friendliness, and low cost. To date, 13 Cu-S compounds have been identified as potential thermoelectric materials.<sup>16,23</sup> Among this group of materials, mawsonite  $\text{Cu}_6\text{Fe}_2\text{SnS}_8$  and stannoidite  $\text{Cu}_8\text{Fe}_3\text{Sn}_2\text{S}_{12}$  were mechanochemically synthesized in a laboratory planetary mill with subsequent spark plasma processing.

Planetary mills are very popular in mechanochemistry, since they enable synthesis of new compounds without the need for bulk dissolution of reactants.<sup>24</sup> Mechanochemistry is rapidly advancing from a laboratory curiosity to a widely industrially used technique.<sup>25–28</sup> One of the main hallmarks of mechanochemistry is its ability to create nanoparticles with well-crystallized core, whereas the near-surface shell regions are disordered (nanostructuring). The process can also be used for preparation of nanostructured materials in scalable amounts.<sup>29</sup>

In addition, nanostructuring has been shown to have a large effect on the thermoelectric performance. A simultaneous increase in the power factor and a decrease in the thermal conductivity in the same nanocomposite was reported.<sup>4</sup> The principal factor behind this performance improvement appears to be increased phonon scattering at interfaces between nanoparticles.<sup>30</sup> Several papers devoted to such nanophenomena have discussed the extent of the different contributions of the power

factor and lattice thermal conductivity to the thermoelectric performance.<sup>12,31–34</sup>

Recently, various papers on the use of the mechanochemical approach to synthesize thermoelectrics have been published.<sup>1,9,16,18,23,34,35</sup> However, all these reports only demonstrated the effectiveness of laboratory-scale mills.

The aim of this work is to investigate the ability of an industrial mill to synthesize quaternary sulfide mawsonite  $\text{Cu}_6\text{Fe}_2\text{SnS}_8$  and compare the thermoelectric performance with samples synthesized in a laboratory planetary mill using elemental precursors.

## EXPERIMENTAL PROCEDURES

### Materials

For the mechanochemical syntheses, copper (99%; Merck, Germany), iron (99%; Winlab, Germany), tin (99%; Nihon Seiko, Japan), and sulfur (99%; CG-Chemikalien, Germany) were used as precursors.

### Processing Techniques

#### *Mechanochemical Synthesis*

Mechanochemical solid-state syntheses were performed in an industrial eccentric vibratory ball mill (ESM 656-0.5 ks, Siebtechnik, Germany) under the following conditions: 5-L steel satellite milling chamber attached to the main corpus of the mill, tungsten carbide balls with diameter of 35 mm and total mass of 25 kg, 80% ball filling, amplitude of the mill of 20 mm, rotational speed of the eccentric of 960  $\text{min}^{-1}$ , argon atmosphere, total feed of reaction precursors of 100 g, and milling time of 5 min to 240 min. Precursors at stoichiometric ratio (6Cu:2Fe:Sn:8S) were used in the batch milling tests. Photographs of the mill together with the attached steel satellite are shown in Fig. 1.

#### *Spark Plasma Sintering*

The powder samples obtained after milling for 30 min and 240 min were placed into a graphite die (inner diameter 15 mm) then sintered at 450°C under 50 MPa with heating rate of 50°C/min and holding time of 5 min in a spark plasma sintering furnace (FCT HPD 25, FCT System GmbH, Germany) in vacuum.

### Characterization Techniques

#### *X-ray Diffractometry (XRD)*

Qualitative identification of the phase composition was performed by XRD analysis using an X'Pert PW 3040 MPD diffractometer (Phillips, Germany) working in Bragg–Brentano geometry with Cu  $\text{K}_{\alpha 1,2}$  doublet radiation.

The XRD patterns of the SPS-treated samples were measured on a Rigaku Ultima IV diffractometer in Bragg–Brentano geometry with fixed slits



Fig. 1. Eccentric vibratory mill with attached satellite (a), and open satellite filled with milling balls (b).

with a Cu  $K_{\alpha 1,2}$  doublet radiation source. The experiment was performed with a mounted HTK1200 N (Anton Paar) high-temperature oven-chamber, which led to an amorphous-type background originating from the chamber windows at low  $2\theta$  angles. This background was estimated by manual determination of background points and linear interpolation between them.

Rietveld refinement of the XRD data was performed using the FullProf program.<sup>36</sup> The XRD line broadening was analyzed by refinement of regular Thompson–Cox–Hastings function parameters. To obtain proper geometry setup and eliminate instrumental broadening, the instrumental resolution function was determined by refinement of the  $\text{LaB}_6$  standard specimen. The Joint Committee on Powder Diffraction Standards (JCPDS) powder diffraction file (PDF) database and Crystallography Open Database implemented in Match! software were utilized for phase identification.

#### Scanning Electron Microscopy (SEM)

SEM images of the samples were recorded using a MIRA 3 field-emission (FE)-SEM microscope (TESCAN, Czech Republic) equipped with an EDX detector (Oxford Instruments, UK).

#### Soxhlet Analysis (SA)

The content of unreacted elemental sulfur in the samples was determined by a simple gravimetric method using a Soxhlet extractor. The extraction thimble was loaded with well-weighed 1 g of powder sample and placed into the main chamber of the extractor. Carbon disulfide (30 mL, 99.9%; Fischer Chemical) was placed into a 500-mL distilling flask, and the apparatus was set up. On heating of the distilling flask in a hot water bath, three cycles were run to quantitatively dissolve all sulfur present in the sample. The resulting solution cooled to room temperature was transferred into a 250-mL round-bottomed flask of known mass, and the solvent was distilled under vacuum. The flask was further dried at 70°C to eliminate any traces of solvent and reweighed.

The degree of conversion  $\alpha$  for the mixture of elements was calculated based on the amount of unconsumed sulfur determined by Soxhlet analysis using the formula

$$\alpha = 1 - \frac{m_{f1} - m_{f0}}{m_{S0}}, \quad (1)$$

where  $\alpha$  is the conversion degree of sulfur,  $m_{S0}$  is the starting amount of sulfur in the reaction mixture per gram,  $m_{f1}$  is the mass of the flask after extraction, and  $m_{f0}$  is the mass of the flask before extraction.

#### Specific Surface Area Measurements

The specific surface area  $S_{\text{BET}}$  was determined by the Brunauer–Emmett–Teller (BET) method using low-temperature nitrogen adsorption in a Gemini 2360 sorption apparatus (Micromeritics, USA).

#### Magnetic Measurements

Magnetic measurements were performed using a MPMS-XL-5 magnetic property measuring system (Quantum Design, USA). Room-temperature magnetic hysteresis loops of mechanochemically synthesized samples were collected up to a maximum applied field of 50 kOe.

#### Thermoelectric Measurements

The temperature-dependent electrical resistivity and Seebeck coefficient were measured using a commercial instrument (LSR-3/110, Linseis) in He atmosphere. The error on the resistivity and Seebeck coefficient measurements is less than 5%. The temperature-dependent thermal diffusivity  $\lambda$  was measured by laser flash method (LFA-457, Netzsch) under Ar. The repeatability of the measurement was better than 2%, while the error on the thermal diffusivity was less than 5%. The specific heat  $C_p$  was calculated (0.49 J/g·K) using the Dulong–Petit law to avoid the large uncertainty in the routine differential scanning calorimetry method. The

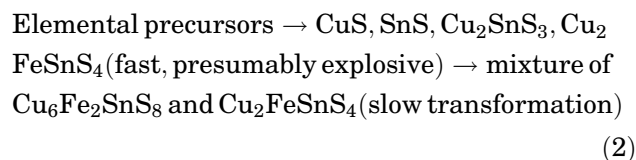
density  $d$  was calculated using the mass and volume of the sintered pellets, yielding values of  $4.55 \text{ g cm}^{-3}$  (relative density > 95%) for the sample milled for 30 min and  $4.22 \text{ g cm}^{-3}$  (relative density 91%) for the sample milled for 240 min. The thermal conductivity was determined using the equation  $\kappa = \lambda C_p d$ . The electrical contribution to the thermal conductivity was estimated using the Wiedemann–Franz law.

## RESULTS AND DISCUSSION

### Structural Analysis of Samples

Due to the thermodynamic aspects of the multi-component system, several intermediate phases form during the course of the reaction; These can be tracked by x-ray diffractometry. Based on the XRD patterns of the samples milled for different times (Fig. 2), we propose the reaction scheme in Eq. 2. After only 5 min of milling, no diffraction peaks assigned to free elements were observed in the diffraction pattern. Rapid conversion of free elements (especially copper) to binary sulfides has been observed by our group before.<sup>37</sup> This is connected to the very low Gibbs energies of formation of binary sulfides. The reflections for CuS (covellite) and SnS (herzenbergite) phases were identified, as highlighted in Fig. 2. The presence of the thermodynamically very stable phase  $\text{Cu}_2\text{SnS}_3$  is evident at the early stage of the reaction with the peak detected at  $28.44^\circ$ . Formation of  $\text{Cu}_2\text{SnS}_3$  has often been observed in the Cu–Sn–S system, besides formation of binary phases.<sup>38</sup> Small amounts of other tertiary/quaternary Cu–Sn–S phases with even lower enthalpies of formation may hypothetically be

present as well.<sup>39</sup> Thus, the following reaction scheme is proposed:



On further milling of the reaction mixture, a gradual decrease in the integral intensity of the CuS and SnS reflections was observed, and the peak formerly at  $28.44^\circ$  shifted slightly to higher  $2\theta$  values. This shift may provide evidence of formation of mawsonite  $\text{Cu}_6\text{Fe}_2\text{SnS}_8$  phase, with the (201) reflection appearing at  $28.80^\circ$ . Because of the extensive amorphization of the material, no other intermediate phases could be identified from the patterns after 240 min of milling. Despite this, other ternary (chalcopyrite, bornite) and quaternary phases (stannite, rhodostannite, stannoidite) may be present in the system.

The Rietveld refinement was performed to determine the phase composition of the sintered samples. Based on the qualitative analysis, chalcopyrite  $\text{CuFeS}_2$  and bornite  $\text{Cu}_5\text{FeS}_4$  were included as major impurities in the refinement along with the mawsonite phase. The starting model proposed by Szymanski et al. was used to refine the mawsonite crystal structure (space group  $P-4m2$ ;  $a \approx 7.61 \text{ \AA}$ ,  $c \approx 5.36 \text{ \AA}$ ).<sup>40</sup> Poor results were obtained for both samples with conventional Rietveld factor  $R_{\text{wp}}$  over 22%. This suggests the possible presence of other phase(s) with structure close to that of mawsonite. Introduction of stannite ( $\text{Cu}_2\text{FeSnS}_4$ ) phase into the refinement led to a significant improvement of the fit with  $R_{\text{wp}}$  factor of 12% to 13%. The refinement results are shown in Fig. 3. The cell parameters calculated for mawsonite (see Supplementary Electronic Material) are in agreement with those reported by Szymanski. This observation leads to the conclusion that pure mawsonite phase can be obtained by ball milling only up to some extent and that detailed structural characterization must be performed for materials prepared from the Cu–Fe–Sn–S system. Even though the stannite phase is also present in a considerable amount, both samples contained over 50% of mawsonite, as further indicated by the good thermoelectric properties described below.

### Sulfur Conversion and Specific Surface Analysis

The results of the unconsumed sulfur analysis were in good agreement with the XRD results for the as-milled samples. Rapid conversion of sulfur to binary and tertiary sulfides at the very beginning of the reaction was observed. After only 15 min of milling, almost no sulfur was present in the sample, and it is thought to be completely consumed.

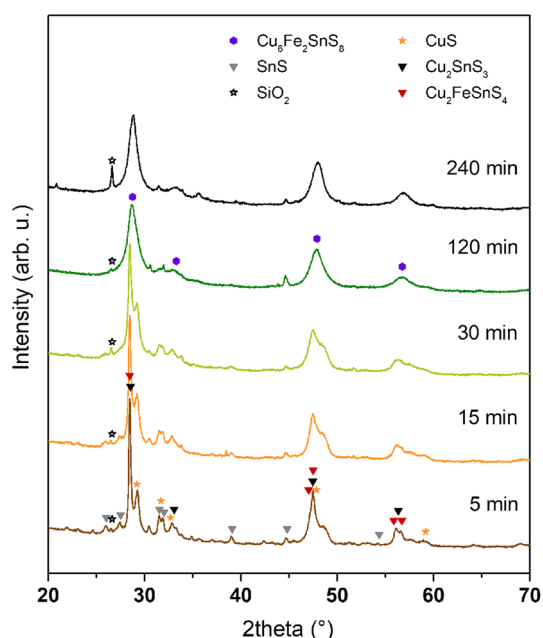


Fig. 2. XRD patterns of reaction mixture milled for various times.

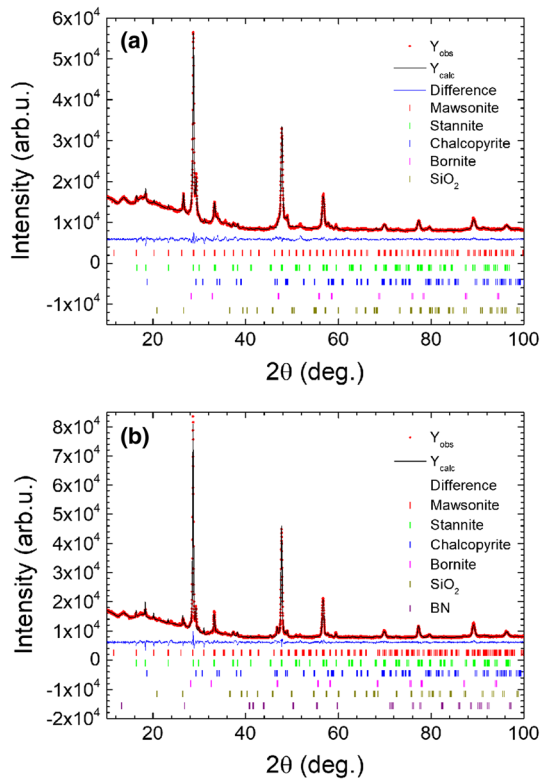


Fig. 3. Rietveld results for samples milled for 30 min (a) and 240 min (b) after SPS treatment.

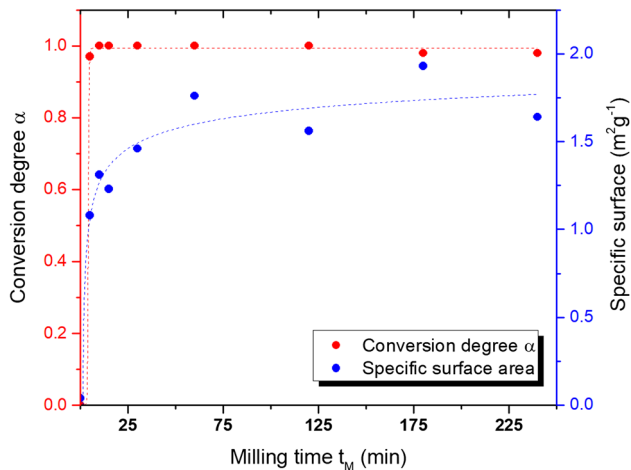


Fig. 4. Sulfur conversion degree  $\alpha$  and specific surface area  $S_{\text{BET}}$  of samples as a function of milling time  $t_M$ .

Figure 4b also shows the BET surface area values. In comparison with the initial value for the non-milled stoichiometric reaction mixture ( $S_{\text{BET}} = 0.24 \text{ m}^2 \text{ g}^{-1}$ ), all the other values are four to eight times higher. The increase in the surface area is strongest at the beginning of the synthesis. As a consequence, formation of fresh surface led to formation of reactive surface sites, which together with the increase in bulk disorder contributes to the high reactivity.

## Morphological Analysis of Powders

SEM analysis is a useful tool to follow the evolution of the size and shape of particles under the effect of high-energy milling. The effects of comminution on agglomeration of binary and ternary sulfides has been studied many times.<sup>29</sup> The morphology of particles milled for 30 min and 240 min is shown in Fig. 5. The population of smaller and larger micrograins can be seen, with a tendency to form agglomerates. In spite of the large difference in treatment time, the overall pictures are not very different. This fact is a consequence of agglomeration supported by small differences in values of the specific surface area:  $S_{\text{BET}} = 1.5 \text{ m}^2 \text{ g}^{-1}$  and  $1.6 \text{ m}^2 \text{ g}^{-1}$  for the samples milled for 30 min and 240 min, respectively (Fig. 5a and b). EDX analysis (Fig. 5d) was used to investigate the presence and atomic percentage of elements in the sample. The formula  $\text{Cu}_{5.22}\text{Fe}_{1.83}\text{Sn}_{1.00}\text{S}_{7.83}$  calculated from spectrum 5 corresponds approximately to the stoichiometric ratio used in the input composition of the reaction mixture but gives no clear evidence of formation of pure mawsonite phase.

## Morphological Analysis of SPS-Densified Samples

Both powders were densified using spark plasma sintering (SPS) to prepare suitable input for thermoelectric measurements (see Part 3.4) and for structural analysis (see Part 3.1). SEM images of the sintered samples are shown in Fig. 6. In the case of the sample milled for shorter time (Fig. 6a), more brittle edges can be documented, in contrast to the sample milled for longer time (Fig. 6b), where a more rounded surface can be seen. Thus, the milling time can significantly affect the properties of the final product processed in the same way. In comparison with Fig. 5a and b, the population of very fine particles is significantly reduced.

Figure 7a–c shows the EDS analysis of the sample milled for 30 min (after SPS treatment). Two different fragments were analyzed. Spectrum 7 clearly reveals a region with stoichiometry that does not correspond to mawsonite phase. Thus, the fragment shown must include crystallites of bornite and chalcopyrite, in agreement with the Rietveld refinement results for the SPSed samples. The other fragment (spectrum 10) shows formation of mawsonite with stoichiometry very close to that expected ( $\text{Cu}_6\text{Fe}_2\text{SnS}_8$ ). This observation points to local inhomogeneity of the material, where regions with high and low phase purity may be found. EDS analysis of the sample milled for 240 min followed by SPS treatment is shown in Fig. 7d–f. Three distinct areas were analyzed, and the corresponding EDS spectra together with the atomic percentages of Cu, Fe, Sn, and S are given. Based on these values, the composition in various areas (spectra 1 to 3) was calculated and is presented in Table I (calculation relative to Sn). The composition calculated from

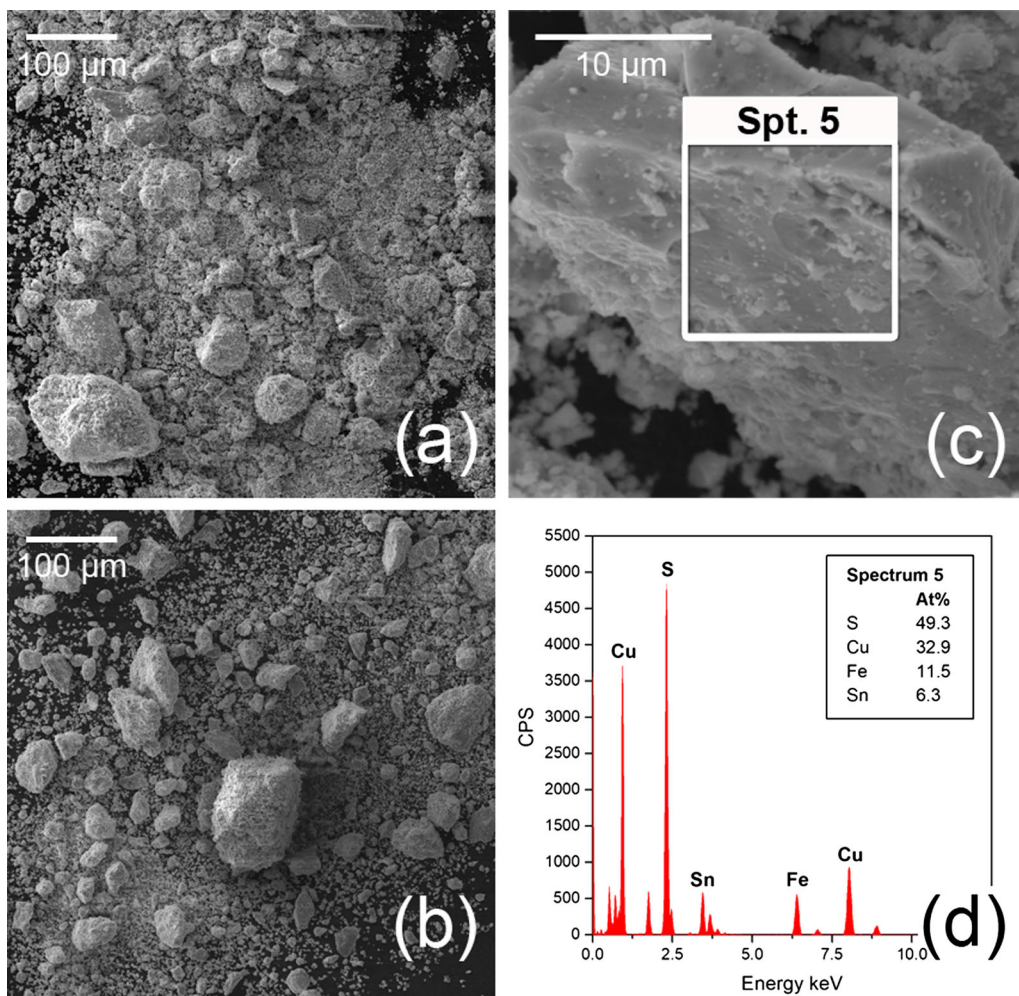


Fig. 5. SEM images and EDS results of samples milled for 30 min (a) and 240 min (b–d), respectively.

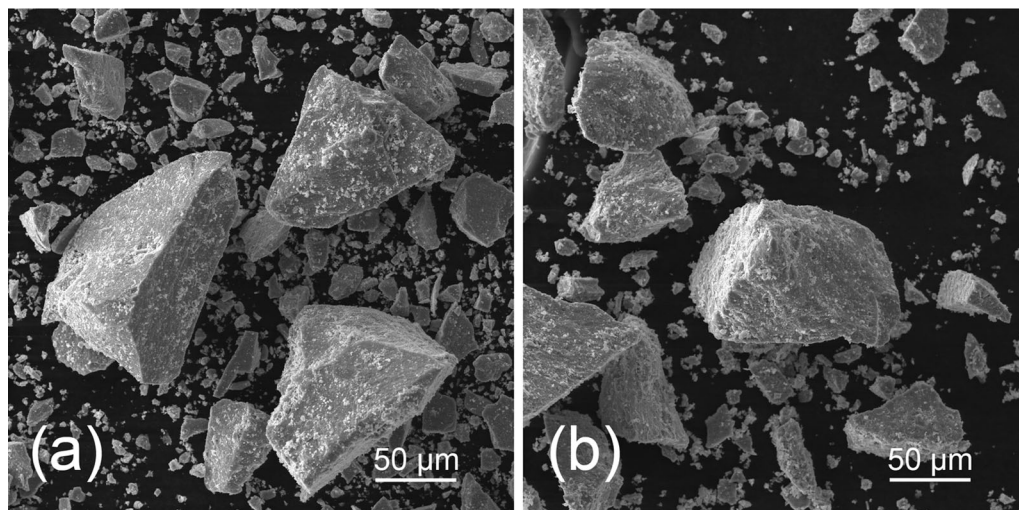


Fig. 6. SEM images of crushed materials after SPS treatment for milling time of (a) 30 min and (b) 240 min.

spectrum 3 deviates slightly from the ideal stoichiometry. However, the material seemed to be more homogeneous compared with the sample

milled for 30 min. No regions with strong deviations from the expected stoichiometry were detected. For comparison, the composition of the sample milled

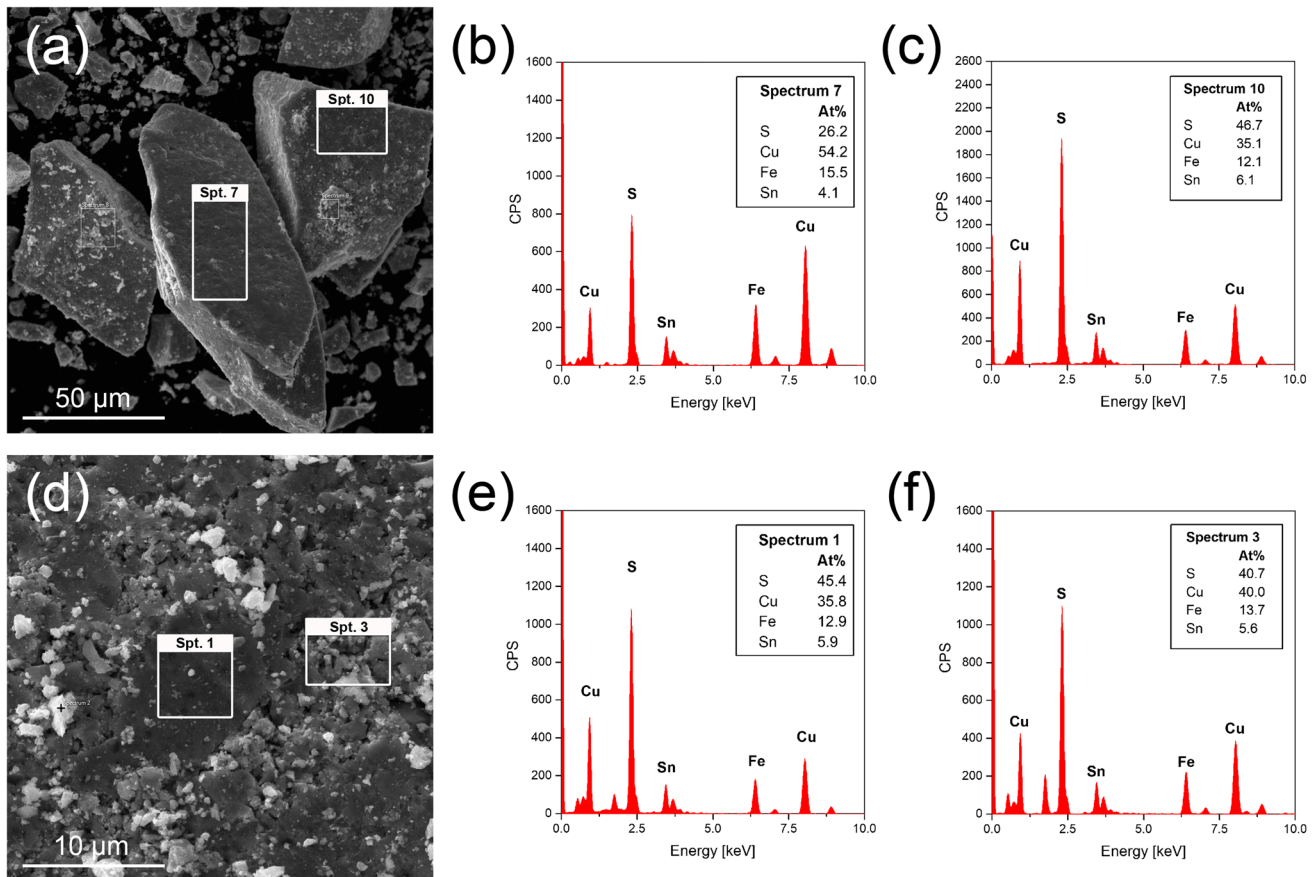


Fig. 7. EDS analysis of samples after SPS treatment for milling time of 30 min (a–c) and 240 min (d–f).

**Table I. Stoichiometry of mawsonite samples calculated from EDS spectra**

	Cu	Fe	Sn	S
Mawsonite	6.00	2.00	1.00	8.00
30 min SPS				
Spectrum 7	13.22	3.78	1.00	6.39
Spectrum 10	5.75	1.98	1.00	7.65
240 min SPS				
Spectrum 1	6.07	2.19	1.00	7.69
Spectrum 2	6.04	2.18	1.00	8.32
Spectrum 3	7.14	2.45	1.00	7.27
240 min				
Spectrum 5	5.22	1.83	1.00	7.83

for 240 min before SPS treatment is also presented in this table (spectrum 5). The EDS results partially showed areas where nanocrystalline mawsonite was formed, but the bulk material seemed to be rather inhomogeneous with low phase purity. Regions where only stannite phase was present were not identified.

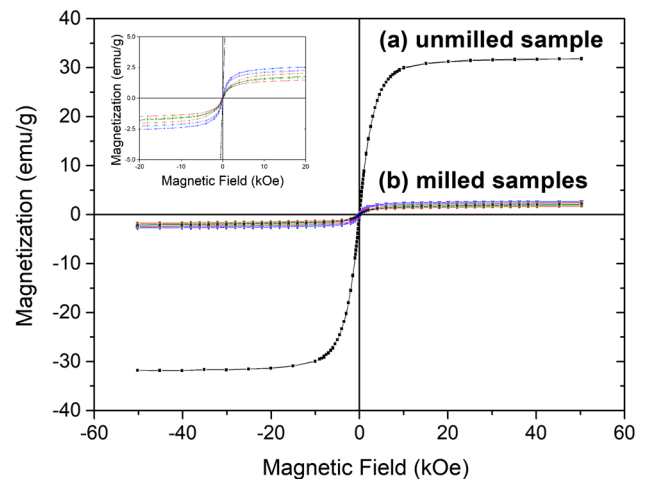


Fig. 8. Magnetic hysteresis loop curves for samples prepared using different milling times: (a) initial mixture of unmilled elements, and (b) samples milled for 5 min, 10 min, 15 min, 30 min, 60 min, 120 min, 180 min, and 240 min (see inset).

### Magnetic Properties

Figure 8 shows the magnetization versus applied field dependence measured at 300 K for the initial mixture of (a) unmilled “free elements” and (b) for

the set of samples subjected to milling for different times. The  $M(H)$  curves are well saturated after application of magnetic fields with magnitude higher than 10 kOe. In principle, these magnetic data can be used for evaluation of the reaction course, because the products are mostly paramagnetic (weakly magnetic).<sup>41</sup> The only strongly magnetic substance is the ferromagnetic iron in the initial mixture of unmilled elements. Therefore, differences in the saturation magnetization of the samples milled for different times are mainly caused by the different amounts of unconsumed iron in these materials at 300 K. The saturation magnetization rapidly decreased to negligible values after milling for only 5 min then remained nearly constant up to milling for 240 min, indicating that most of the elemental Fe was consumed by the mechanochemical reaction in the early stages of the milling process. This observation is in very good agreement with the sulfur consumption results shown in Fig. 4. Moreover, such fast consumption of elemental iron supports the formation of binary Fe-S and tertiary Cu-Fe-S sulfides as also observed in the XRD patterns.

### Thermoelectric Properties

Figure 9 shows the thermoelectric properties of the sample milled for 240 min after SPS treatment. The electrical conductivity (Fig. 9a) shows

semiconducting behavior. Hole carriers may be created by Sn deficiency, which is supported by the EDS results in Table I and a previous study on stannoidite  $\text{Cu}_8\text{Fe}_3\text{Sn}_2\text{S}_{12}$ .<sup>18</sup> As  $\text{Sn}^{4+}$  has  $4d^{10}$  configuration and does not contribute to hole transport, hole carriers are transported in the Cu-S tetrahedral network. Sn vacancies create a shallow acceptor level slightly above the valence-band maximum,<sup>42</sup> and with increasing temperature, more holes in the Sn defect level are excited into the valence band, improving the electrical conductivity and resulting in the semiconductor behavior. Greater Sn deficiency could thus lead to an increase in the electrical conductivity (Fig. 9a) compared with mawsonite prepared in the previous study of Zhang et al.<sup>16</sup> Also, since our samples are multiphase, it is worth comparing the experimental data with data already published on pure samples. x-Ray powder diffraction (XRPD) experiments detected that the highest chemical fraction (55 wt.% to 59 wt.%) in our samples belongs to mawsonite and the second highest chemical fraction (32 wt.% to 36 wt.%) belongs to stannite. Previously published data report the electrical conductivity of stannite to be on the order of 0.01 S/cm at temperatures above room temperature.<sup>43</sup> Thus, the electrical conductivity of our samples cannot be significantly affected by the stannite phase. On the other hand, the mawsonite sample prepared by Zhang et al. exhibited conductivity comparable to ours (see

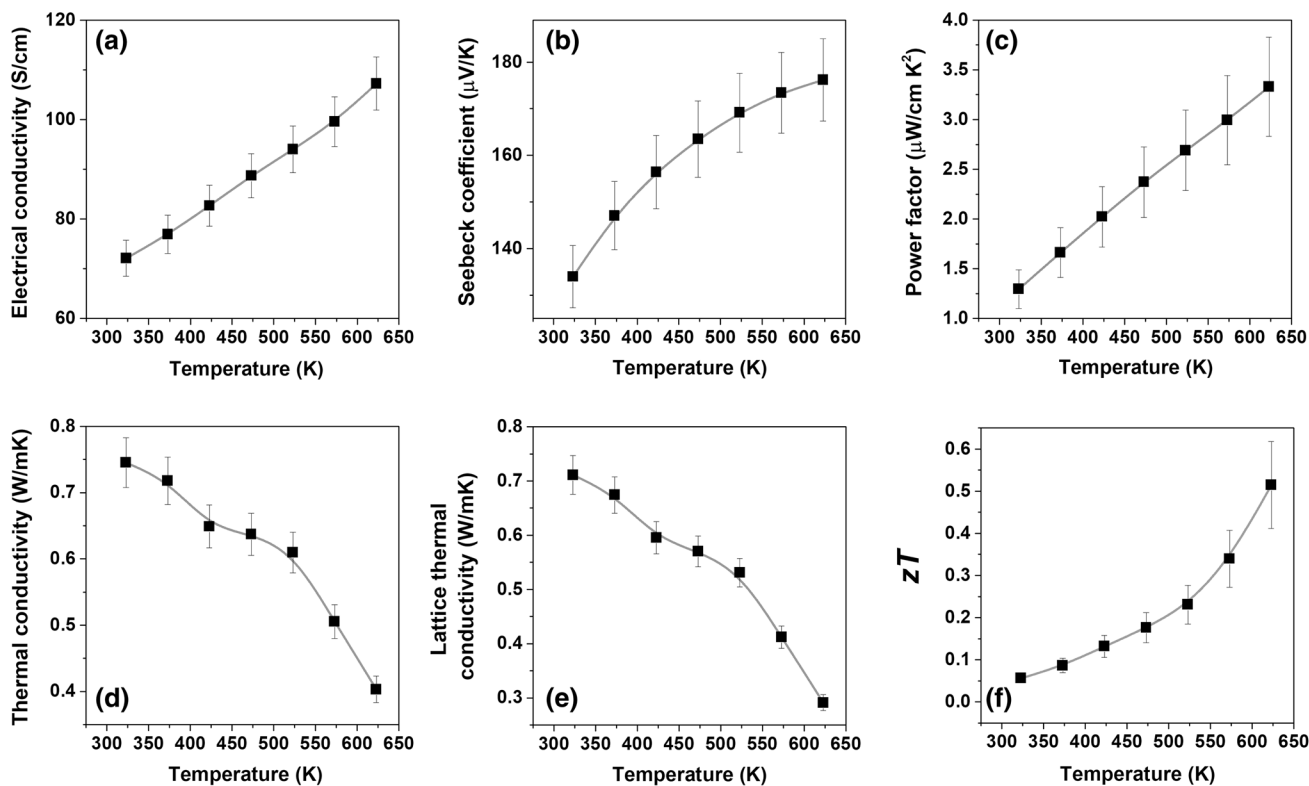


Fig. 9. Thermoelectric properties of the sample milled for 240 min after SPS treatment in the range of 325 K to 625 K: (a) electrical conductivity, (b) Seebeck coefficient, (c) power factor, (d) thermal conductivity, (e) lattice thermal conductivity, and (f)  $zT$ .



Supplementary Fig. S1). Since both our group and Zhang et al. performed experiments on pressed and sintered powders, the absolute values are strongly affected by the intergrain conductivity, which can serve as another explanation for the 10% discrepancy in the obtained data. The remaining two impurities are chalcopyrite and bornite, with only a minor fraction of 4.5 wt.% to 6.8 wt.% and 2 wt.% to 4.7 wt.%, respectively. These compounds exhibit electrical conductivity one order of magnitude lower<sup>22,44</sup> than we measured. For these reasons, we estimate that neither of these two phases contributed significantly to the total electrical conductivity of the samples. In conclusion, the electrical conductivity is mostly driven by the electrical conductivity of mawsonite phase.

The density of the SPS-treated sample reported in a previous study<sup>16</sup> was nearly the same as for the sample milled for 30 min in this work, and they both showed local inhomogeneity with bornite and chalcopyrite. As the sample milled for 240 min was more homogeneous according to the EDS results in Fig. 6, the carrier mobility should be larger in this sample, hence the electrical conductivity was slightly improved.

It is interesting to compare the thermoelectric properties of mawsonite  $\text{Cu}_6\text{Fe}_2\text{SnS}_8$  with those of the other two compounds, i.e., stannoidite  $\text{Cu}_8\text{Fe}_3\text{Sn}_2\text{S}_{12}$  and stannite  $\text{Cu}_2\text{FeSnS}_4$ , as all three compounds consist of the same elements. They all have Cu-S tetrahedral network as hole conducting channel (see Supplementary Fig. S2 for the crystal structures of mawsonite and stannite), so their band structure and power factor can be analyzed and compared using a recently proposed descriptor<sup>45</sup> for chalcopyrite compounds:  $\eta = c/2a$ , where  $c$  and  $a$  are lattice parameters and  $\eta$  approaching unity means higher power factor. By some crystal lattice transformation, the descriptors were calculated as 0.95 for mawsonite, 0.99 for stannoidite, and 0.98 for stannite. Based on these results, it seems that high power factor can be obtained for stannoidite, which is supported by literature showing that the highest reported power factor in these three compounds is  $6 \mu\text{W}/\text{cm}\cdot\text{K}^2$  for stannoidite  $\text{Cu}_{8.3}\text{Fe}_{2.7}\text{Sn}_2\text{S}_{12}$ .<sup>18</sup> Meanwhile, the hyperstoichiometric compound mawsonite shows the highest power factor of  $3.3 \mu\text{W}/\text{cm}\cdot\text{K}^2$  (Fig. 9c) because of its much higher electrical conductivity compared with the other two compounds. Specifically, the electrical conductivity values from room temperature up to 670 K are 13 S/cm to 25 S/cm for stannoidite<sup>18</sup> and 10 S/cm to 30 S/cm for stannite.<sup>46</sup> According to our results, the conductivity of mawsonite phase must be significantly higher (Fig. 9a). This also contributed to the improvement of the power factor reported herein. It seems that, in mawsonite, Sn vacancies are more effective for providing carriers, resulting in higher carrier concentration and hence higher electrical conductivity, which is worth further investigation.

The lattice thermal conductivity is very low, below 1 W/m-K, over the whole temperature range, and reaches 0.29 W/m-K at 623 K (Fig. 9e). There are two reasons for this low thermal conductivity. Firstly, the weak bonding of copper atoms can lead to an unexpected vibrational mode at low frequencies,<sup>47</sup> which is likely to be a major contributor. Secondly, mechanochemical synthesis using ball milling plus spark plasma sintering produces ceramics with fine grain size,<sup>48,49</sup> in which phonon scattering centers such as grain boundaries will further reduce the lattice thermal conductivity. Compared with the very low lattice thermal conductivity of some similar Cu-S-based compounds, e.g., colusite  $\text{Cu}_{26}\text{Ge}_2\text{M}_6\text{S}_{32}$ <sup>50</sup> ( $\sim 0.3$  W/m-K at 663 K) and tetrahedrite  $\text{Cu}_{11.5}\text{Zn}_{0.5}\text{Sb}_4\text{S}_{13}$ <sup>8</sup> ( $\sim 0.2$  W/m-K at 673 K), the low thermal conductivity of mawsonite is not surprising. The  $zT$  value reached 0.51 at 623 K (Fig. 9f) due to the very low lattice thermal conductivity (0.29 W/m-K) and moderate power factor ( $3.3 \mu\text{W}/\text{cm}\cdot\text{K}^2$ ).

## CONCLUSIONS

Nanobulk mawsonite ( $\text{Cu}_6\text{Fe}_2\text{SnS}_8$ )/stannite ( $\text{Cu}_2\text{FeSnS}_4$ ) composite containing minor amounts of chalcopyrite ( $\text{CuFeS}_2$ ) and bornite ( $\text{Cu}_5\text{FeS}_4$ ) was synthesized using an industrial eccentric vibration mill. Milling was performed up to 240 min in argon atmosphere using Cu, Fe, Sn, and S as elemental precursors. XRD, EDS, SEM, and Soxhlet extraction, nitrogen adsorption, magnetic, and thermoelectric measurements were used to characterize the bulk, surface, magnetic, and thermoelectric properties of the synthesized products. The transformation of the elemental precursors to a composite mixture proceeded relatively rapidly via several intermediate steps. XRD analysis detected binary phases from the Cu-S and Fe-S systems. It is presumed that  $\text{Cu}_2\text{SnS}_3$  phase forms at the very beginning of the reaction as well, due to its low Gibbs energy of formation. Rietveld analysis of the SPS-treated samples revealed formation of a composite mixture containing over 50% mawsonite phase and nearly 40% stannite. Thermoelectric measurements on the sample milled for 240 min revealed a figure of merit  $zT$  of 0.51 at 623 K. This high  $zT$  value originates from the low lattice thermal conductivity of 0.29 W/m-K and moderate power factor of  $3.3 \mu\text{W}/\text{cm}\cdot\text{K}^2$ . The  $zT$  value obtained for this sample, synthesized in an industrial mill, is comparable to values obtained for samples referred to as pure mawsonite prepared using a laboratory ball mill. Some parameters are, however, slightly improved.

The synthesized composite mixture of two quaternary sulfides represents a perspective thermoelectric material for future applications. The material itself comprises only nontoxic and Earth-abundant components. As shown by these results,

this mechanochemical approach utilizing an industrial mill can serve as a scalable route for preparation of thermoelectric materials. As well as demonstrating the scalability of this mawsonite synthesis approach, detailed inspection of the prepared materials by the Rietveld analysis revealed formation of a composite mixture, resulting in small discrepancies from results published previously by Zhang et al. The importance of advanced structural characterization for compounds from the quaternary Cu-Fe-Sn-S system is thus highlighted.

### ACKNOWLEDGMENTS

This work was supported by the projects of the Slovak Research and Development Agency APVV (VV-0103-14), Slovak Grant Agency VEGA (2/0044/18, 2/0065/18), and ITMS 26220120035. The support of European Project COST (OC-2015-1-19345) is also acknowledged.

### ELECTRONIC SUPPLEMENTARY MATERIAL

The online version of this article (<https://doi.org/10.1007/s11664-019-06972-7>) contains supplementary material, which is available to authorized users.

### REFERENCES

1. K. Chen, B.L. Du, N. Bonini, C. Weber, H.X. Yan, and M.J. Reece, *J. Phys. Chem. C* 120, 27135 (2016).
2. S. Hebert, D. Berthebaud, R. Daou, Y. Breard, D. Pelloquin, E. Guilmeau, F. Gascoin, O. Lebedev, and A. Maignan, *J. Phys. Condens. Matter* 28, 013001 (2016).
3. X. Zhang and L.D. Zhao, *J. Materiomics* 1, 92 (2015).
4. M.S. Dresselhaus, G. Chen, M.Y. Tang, R.G. Yang, H. Lee, D.Z. Wang, Z.F. Ren, J.P. Fleurial, and P. Gogna, *Adv. Mater.* 19, 1043 (2007).
5. H.J. Goldsmid, *Introduction to Thermoelectricity* (Berlin: Springer, 2010).
6. K. Suekuni, K. Tsuruta, T. Ariga and M. Koyano, *Appl. Phys. Express* 5, article ID 051201 (2012).
7. K. Suekuni, K. Tsuruta, M. Kunii, H. Nishiate, E. Nishibori, S. Maki, M. Ohta, A. Yamamoto and M. Koyano, *J. Appl. Phys.* 113, article ID 043712 (2013).
8. X. Lu, D.T. Morelli, Y. Xia, F. Zhou, V. Ozolins, H. Chi, X.Y. Zhou, and C. Uher, *Adv. Energy Mater.* 3, 342 (2013).
9. X. Lu and D.T. Morelli, *Phys. Chem. Chem. Phys.* 15, 5762 (2013).
10. C.M. Fella, Y.E. Romanyuk, and A.N. Tiwari, *Sol. Energy Mater. Sol. Cells* 119, 276 (2013).
11. K. Suekuni and T. Takabatake, *APL Mater.* 4, 104503 (2016).
12. S. Fasolin, S. Fiameni, C. Fanciulli, S. Battiston, A. Farnengo, and M. Fabrizio, *J. Nanosci. Nanotechnol.* 17, 1645 (2017).
13. P. Baláž and M. Achimovičová, *Int. J. Miner. Process.* 81, 44 (2006).
14. P. Baláž, M. Achimovičová, J. Ficeriová, R. Kammel, and V. Šepelák, *Hydrometallurgy* 47, 297 (1998).
15. M. Rull-Bravo, A. Moure, J.F. Fernandez, and M. Martin-Gonzalez, *RSC Adv.* 5, 41653 (2015).
16. R.Z. Zhang, K. Chen, B. Du, and M.J. Reece, *J. Mater. Chem. A* 5, 5013 (2017).
17. B.L. Du, R.Z. Zhang, K. Chen, A. Mahajan, and M.J. Reece, *J. Mater. Chem. A* 5, 3249 (2017).
18. V.P. Kumar, T. Barbier, V. Caignaert, B. Raveau, R. Daou, B. Malaman, G. Le Caer, P. Lemoine, and E. Guilmeau, *J. Phys. Chem. C* 121, 16454 (2017).
19. C. Bourges, M. Gilmas, P. Lemoine, N.E. Mordvinova, O.I. Lebedev, E. Hug, V. Nassif, B. Malaman, R. Daou, and E. Guilmeau, *J. Mater. Chem. C* 4, 7455 (2016).
20. C. Bourges, Y. Bouyrie, A.R. Supka, R.A. Al Orabi, P. Lemoine, O.I. Lebedev, M. Ohta, K. Suekuni, V. Nassif, V. Hardy, R. Daou, Y. Miyazaki, M. Fornari, and E. Guilmeau, *JACS* 140, 2186 (2018).
21. G. Guelou, A.V. Powell, and P. Vaquero, *J. Mater. Chem. C* 3, 10624 (2015).
22. S.O.J. Long, A.V. Powell, P. Vaquero, and S. Hull, *Chem. Mater.* 30, 456 (2018).
23. V.P. Kumar, L. Paradis-Fortin, P. Lemoine, V. Caignaert, B. Raveau, B. Malaman, G. Le Caer, S. Cordier, and E. Guilmeau, *Inorg. Chem.* 56, 13376 (2017).
24. P. Baláž, M. Achimovičová, M. Baláž, P. Billik, Z. Cherkezova-Zheleva, J.M. Criado, F. Delogu, E. Dutková, E. Gaffet, F.J. Gotor, R. Kumar, I. Mitov, T. Rojac, M. Senna, A. Streletskii, and K. Wieczorek-Ciurowa, *Chem. Soc. Rev.* 42, 7571 (2013).
25. S.L. James, C.J. Adams, C. Bolm, D. Braga, P. Collier, T. Friščić, F. Grepioni, K.D.M. Harris, G. Hyett, W. Jones, A. Krebs, J. Mack, L. Maini, A.G. Orpen, I.P. Parkin, W.C. Shearouse, J.W. Steed, and D.C. Waddell, *Chem. Soc. Rev.* 41, 413 (2012).
26. S.L. James and T. Friscic, *Chem. Soc. Rev.* 42, 7494 (2013).
27. W. Jones and M.D. Eddleston, *Faraday Discuss.* 170, 9 (2014).
28. J.L. Do and T. Friščić, *ACS Central Sci.* 3, 13 (2017).
29. P. Baláž and E. Dutková, *Miner. Eng.* 22, 681 (2009).
30. P. Vaquero and A.V. Powell, *J. Mater. Chem.* 20, 10950 (2010).
31. M.G. Kanatzidis, *Chem. Mater.* 22, 648 (2010).
32. J.P. Heremans, M.S. Dresselhaus, L.E. Bell, and D.T. Morelli, *Nat. Nanotechnol.* 8, 471 (2013).
33. G.J. Snyder and E.S. Toberer, *Nat. Mater.* 7, 105 (2008).
34. S.K. Bux, R.G. Blair, P.K. Gogna, H. Lee, G. Chen, M.S. Dresselhaus, R.B. Kaner, and J.P. Fleurial, *Adv. Funct. Mater.* 19, 2445 (2009).
35. T. Barbier, S. Rollin-Martin, P. Lemoine, F. Gascoin, A. Kaltzoglou, P. Vaquero, A.V. Powell, and E. Guilmeau, *J. Am. Ceram. Soc.* 99, 51 (2016).
36. J. Rodriguez-Carvajal, LLB Sacley LCSIM Rennes. Fr. (2003).
37. M. Baláž, A. Zorkovská, F. Urakaev, P. Baláž, J. Briančin, Z. Bujňáková, M. Achimovičová, and E. Gock, *RSC Adv.* 6, 87836 (2016).
38. W. Bao and M. Ichimura, *Int. J. Photoenergy*, article ID 592079 (2015).
39. P.W. Guan, S.L. Shang, G. Lindwall, T. Anderson, and Z.K. Liu, *Sol. Energy* 155, 745 (2017).
40. J.T. Szymanski, *Can. Mineral.* 14, 529 (1976).
41. T. Yamanaka, *Am. Mineral.* 61, 260 (1976).
42. X.L. Zhang, M.M. Han, Z. Zeng, and H.Q. Lin, *RSC Adv.* 6, 15424 (2016).
43. V.S. Zakhvalinskii, T.T.H. Nguyen, T.T. Pham, N.T. Dang, E.A. Piliuk, and S.V. Taran, *J. Electron. Mater.* 46, 3523 (2017).
44. B. Donovan and G. Reichenbaum, *Br. J. Appl. Phys.* 9, 474 (1958).
45. J.W. Zhang, R.H. Liu, N.A. Cheng, Y.B. Zhang, J.H. Yang, C. Uher, X. Shi, L.D. Chen, and W.Q. Zhang, *Adv. Mater.* 26, 3848 (2014).
46. C. Xiao, K. Li, J.J. Zhang, W. Tong, Y.W. Liu, Z. Li, P.C. Huang, B.C. Pan, H.B. Su, and Y. Xie, *Mater. Horiz.* 1, 81 (2014).

47. P. Vaqueiro, R.A.R. Al Orabi, S.D.N. Luu, G. Guelou, A.V. Powell, R.I. Smith, J.P. Song, D. Wee, and M. Fornari, *Phys. Chem. Chem. Phys.* 17, 31735 (2015).
48. Z.H. Ge, B.P. Zhang, Y.X. Chen, Z.X. Yu, Y. Liu, and J.F. Li, *Chem. Commun.* 47, 12697 (2011).
49. J. Wu, F. Li, T.R. Wei, Z.H. Ge, F.Y. Kang, J.Q. He, and J.F. Li, *J. Am. Ceram. Soc.* 99, 507 (2016).
50. K. Suekuni, F.S. Kim, H. Nishiate, M. Ohta, H.I. Tanaka and T. Takabatake, *Appl. Phys. Lett.* 105, article ID 132107 (2014).